







## PAPER

[View Article Online](#)  
[View Journal](#) | [View Issue](#)Cite this: *Nanoscale Adv.*, 2024, 6, 4247

## Mn-ferrite nanoparticles as promising magnetic tags for radiofrequency inductive detection and quantification in lateral flow assays†

Vanessa Pilati, \*<sup>ab</sup> María Salvador, <sup>ac</sup> Leyre Bei Fraile,<sup>a</sup> José Luis Marqués-Fernández,<sup>a</sup> Franciscarlos Gomes da Silva, <sup>b</sup> Mona Fadel, <sup>a</sup> Ricardo López Antón,<sup>d</sup> María del Puerto Morales, <sup>c</sup> José Carlos Martínez-García<sup>ae</sup> and Montserrat Rivas <sup>ae</sup>

Lateral flow assays are low-cost point-of-care devices that are stable, easy to use, and provide quick results. They are mostly used as qualitative screening tests to detect biomarkers for several diseases. Quantification of the biomarkers is sometimes desirable but challenging to achieve. Magnetic nanoparticles can be used as tags, providing both visual and magnetic signals that can be detected and quantified by magnetic sensors. In the present work, we synthesized superparamagnetic  $\text{MnFe}_2\text{O}_4$  nanoparticles using the hydrothermal coprecipitation route.  $\text{MnFe}_2\text{O}_4$  presents low magnetic anisotropy and high saturation magnetization, resulting in larger initial magnetic susceptibility, which is crucial for optimizing the signal in inductive sensors. We functionalized the coprecipitated nanoparticles with citric acid to achieve colloidal stability in a neutral pH and to provide carboxyl groups to their surface to bioconjugate with biomolecules, such as proteins and antibodies. The nanomaterials were characterized by several techniques, and we correlated their magnetic properties with their sensitivity and resolution for magnetic detection in radiofrequency inductive sensors. We considered the NeutrAvidin/biotin model of biorecognition to explore their potential as magnetic labels in lateral flow assays. Our results show that  $\text{MnFe}_2\text{O}_4$  nanoparticles are more sensitive to inductive detection than magnetite nanoparticles, the most used nanotags in magnetic lateral flow assays. These nanoparticles present high potential as magnetic tags for the development of sensitive lateral flow immunoassays for detecting and quantifying biomarkers.

Received 29th May 2024

Accepted 5th July 2024

DOI: 10.1039/d4na00445k

[rsc.li/nanoscale-advances](https://rsc.li/nanoscale-advances)

## 1. Introduction

Rapid diagnostic tests based on lateral flow assays (LFAs) are paper portable devices that are simple, fast, stable, and inexpensive. They are useful for point-of-care self-testing when well-equipped laboratories are unavailable. LFAs have been used successfully as qualitative screening tests for detecting disease biomarkers, contaminants, and toxins.<sup>1–3</sup>

Classical LFAs combine microfluidics and biorecognition strategies. In brief, a fluid to analyse, which can be a body fluid (blood, saliva, urine, serum, plasma), an environment sample such as wastewater, or a food sample, is deposited into a sample pad. The fluid flows along a nitrocellulose membrane strip by capillary action. The nitrocellulose has a test line containing specific biorecognition molecules that can capture the analyte, which is tagged by a nanolabel to be detected. If an analyte is in the fluid sample, it is trapped at the test line together with the nanolabels. Commercial LFAs are mainly based on gold nanoparticles that provide a reddish colour signal in the test line, which can be interpreted as a positive or negative result.

Quantifying the molecule of interest in the sample is often necessary for the early diagnosis of some illnesses and detecting contaminants and toxins. However, it remains a significant challenge in LFAs that use visible labels. Calibration difficulties arise from ambient lighting variations, humidity, and differences in paper colours. Importantly, in optical sensors, the signal arises mostly from nanolabels in the upper section of the test line, while a significant fraction of them within the paper remains undetected.<sup>4</sup>

<sup>a</sup>Departamento de Física, Campus de Viesques, Universidad de Oviedo, Gijón, 33204, Spain. E-mail: [pilativanessa@uniovi.es](mailto:pilativanessa@uniovi.es)

<sup>b</sup>Complex Fluids Group, Instituto de Física & Faculdade UnB – Planaltina, Universidade de Brasília, Brasília, 70910-900, Brazil

<sup>c</sup>Departamento de Nanociencia y Nanotecnología, Instituto de Ciencia de Materiales de Madrid (ICMM), Madrid, 28049, Spain

<sup>d</sup>Instituto Regional de Investigación Científica Aplicada (IRICA) and Departamento de Física Aplicada, Universidad de Castilla-La Mancha, Ciudad Real, Spain

<sup>e</sup>Instituto Universitario de Tecnología Industrial de Asturias (IUTA), Gijón, 33203, Spain

† Electronic supplementary information (ESI) available: Table ESI 1 – Resulting parameters from the law of approach to saturation fitting for 300 K and 5 K magnetization measurements. See DOI: <https://doi.org/10.1039/d4na00445k>

Magnetic nanoparticles (NPs) may be used as labels to quantify the bio-analytes in the test line. Besides the visual signal, they can be detected by magnetic sensors, which are sensitive to all the NPs through the thickness of the membrane. In addition, manipulating magnetic NPs enables analyte separation in a complex sample and its pre-concentration to further increase the sensitivity.<sup>5–7</sup> Magnetic tags have been used to quantify *Bacillus anthracis* spores,<sup>8</sup> *Streptococcus pneumoniae* biomarkers,<sup>7</sup> cancer biomarkers,<sup>9</sup> drug abuse,<sup>10</sup> and histamine in wine,<sup>11</sup> among others. Most magnetic LFAs are based on superparamagnetic iron oxide, usually magnetite ( $\text{Fe}_3\text{O}_4$ ) nanoparticles and their assemblies.<sup>12</sup>

Several magnetic sensors with different physical principles have been explored to quantify the magnetic nanoparticles in the test line and, therefore, the target biomolecule. They can be mainly classified as magnetoresistive readers or inductive readers.<sup>13,14</sup> The most common magnetoresistive sensors for reading LFAs are based on giant magnetoresistance (GMR)<sup>15–17</sup> and tunnel magnetoresistance (TMR).<sup>18,19</sup> Magneto-inductive sensors have also been used to achieve quantification in LFAs. A superconducting quantum interference device (SQUID) magnetometer is the most sensitive option.<sup>14</sup> However, it demands expensive maintenance and fabrication, hindering its use as a point-of-care sensor. Atomic magnetometers have also been used to achieve high sensitivity in LFAs quantification.<sup>20</sup> Other inductive strategies based on magnetic flux,<sup>21</sup> magnetic permeability<sup>14,22–24</sup> and non-linear magnetization<sup>25</sup> have been developed to be low-cost and easily miniaturized while achieving high sensitivities for the detection of several biomarkers.<sup>14</sup>

In the case of inductive sensors based on magnetic permeability, a copper coil applies an alternating magnetic field to adjacent superparamagnetic particles. The particles increase the coil's self-inductance and resistance, analogous to the effect of a ferrite core on an inductor, and this change in impedance is measured with an impedance analyser.<sup>24,26</sup> The magnetic signal can be optimized by increasing the magnetic permeability of the magnetic material  $\mu = \mu_0(1 + \chi) = B/H$ , being  $\mu_0$  the vacuum magnetic permeability,  $\chi$  the magnetic susceptibility,  $B$  the magnetic induction, and  $H$  the applied magnetic field. This can be achieved by increasing the size of the magnetic material while keeping its superparamagnetic character<sup>27</sup> and also reducing its magnetic anisotropy.

For this work, we chose to investigate the radiofrequency inductive response of manganese-ferrite  $\text{MnFe}_2\text{O}_4$  NPs to be used as magnetic nanolabels in magnetic lateral flow assays instead of the most common magnetite NPs. Bulk Mn-ferrites are soft magnetic materials with a very low magnetocrystalline anisotropy constant<sup>28</sup> ( $K = 0.3 \times 10^4 \text{ J m}^{-3}$ ) compared to that of magnetite ( $1.1 \times 10^4 \text{ J m}^{-3}$ ). Bulk Mn-ferrite has a high specific saturation magnetization at ambient temperature ( $80 \text{ A m}^2 \text{ kg}^{-1}$ ), close to that of magnetite ( $90 \text{ A m}^2 \text{ kg}^{-1}$ ).<sup>28</sup> Therefore,  $\text{MnFe}_2\text{O}_4$  NPs are expected to present a high initial magnetic susceptibility, which is important for detection in inductive sensors. In addition, colloidal dispersions of Mn-ferrite NPs are dark brown/black, while those based on iron oxides like magnetite and maghemite NPs are usually brown/orange, and

those based on gold NPs are red. Therefore, it is expected that Mn-ferrite can provide better optical contrast between the test line and the paper background compared to pure iron-oxide and gold NPs.

Several techniques can be used to synthesize Mn-ferrites nanoparticles, mostly based on “bottom-up” chemical approaches. The most common methods are coprecipitation,<sup>29,30</sup> thermal decomposition,<sup>31,32</sup> solvothermal,<sup>33</sup> and hydrothermal methods.<sup>34</sup> In this paper, we synthesized Mn-ferrite NPs using a hydrothermal coprecipitation route. It consists of the simultaneous precipitation of  $\text{Fe}^{3+}$  and  $\text{Mn}^{2+}$  in alkaline media under constant heating and stirring. Such a technique has a high yield at low cost and complexity. It does not require the use of highly toxic solvents or surfactants. Both aspects make hydrothermal coprecipitation a promising technique for industrial and commercial purposes. However, the control over size and shape is generally limited. Several parameters can potentially modify the final coprecipitated NPs. These include the nature and concentration of the metallic precursors<sup>35</sup> and of the alkaline base,<sup>29,30</sup> the reaction temperature,<sup>36</sup> the stirring rate<sup>37</sup> and the experimental setup. The control of these parameters is crucial for optimizing NP properties and ensuring reproducibility.

The coprecipitated NPs of the present work were functionalized with citric acid to achieve colloidal stability at neutral pH and provide carboxyl groups at the NP surface for their bio-conjugation. We investigated the detection performance of our NPs using a radiofrequency inductive sensor and compared their magnetic signal with their magnetic properties. In addition, the NPs with higher sensitivity were bioconjugated with NeutrAvidin to test their performance as magnetic labels in lateral flow assays composed of a biotin-bovine-serum-albumin (biotin-BSA) test line in a well-known biochemistry NeutrAvidin-biotin model of biorecognition.

## 2. Experimental section

### 2.1. Chemicals

Manganese(II) chloride tetrahydrate, iron(III) chloride hexahydrate, methylamine 40%, and citric acid were purchased from Sigma-Aldrich (Spain). Hydrochloric acid 37% was obtained from Scharlau (Spain). All chemicals were analytical grade and were used without further treatment or purification. NeutrAvidin protein was purchased from Invitrogen – Thermo Fischer Scientific (USA). 1-Ethyl-3-[3-di-methylpropyl] carbodiimide (EDC) was obtained from Thermo Scientific (Germany). Biotin-conjugated bovine serum albumin (biotin-BSA), bovine serum albumin (BSA), and Tween 20 (polysorbate 20) were obtained from Sigma-Aldrich (Spain). We used deionized water for the solutions preparation and washing steps.

Lateral flow strips were prepared using a nitrocellulose membrane (UniSart CN95) from Sartorius Stedim Biotech (Spain), an absorbent pad (Whatman CF5) from GE Healthcare Life Sciences (UK), a backing card (HF000MC100) and a glass fiber sample pad (GFCP001000) from Millipore (USA). All components of the lateral flow strips were used without further modifications.



## 2.2 Samples preparation

Two samples based on citric acid-coated Mn-ferrite NPs were obtained by a two-step procedure:

**Synthesis of Mn-ferrite NPs.** First, we synthesized  $\text{MnFe}_2\text{O}_4$  NPs using a hydrothermal coprecipitation method.<sup>30</sup> In brief, we prepared a mixture containing 166 mL of  $\text{MnCl}_2$  (0.5 M), 333 mL of  $\text{FeCl}_3$  (0.5 M) and 166 mL of HCl (2.0 M) solutions with 1335 mL of deionized water. This mixture was heated with constant mechanical stirring until boiling ( $\sim 95^\circ\text{C}$ ). We quickly added 250 mL of  $\text{CH}_3\text{NH}_2$  (40%) solution to the boiling mixture, and the reaction continued for 30 minutes, with constant heating and mechanical stirring. We used two stirring rates (low – 170 rpm and medium – 360 rpm) to obtain two samples with different NP diameters, following what is known in literature.<sup>37,38</sup> Samples were named S1 (360 rpm) and S2 (170 rpm). After the end of the reaction, we washed the magnetic precipitate several times with deionized water and subsequent magnetic separation.

**Functionalization with citric acid and peptization.** We added 3.0 g of citric acid powder directly in the aqueous magnetic precipitate with 250 mL of deionized water with a pH of 10. The mixture was then heated and maintained at  $95^\circ\text{C}$  for 20 minutes while vigorously stirring. The adsorption of citric acid onto the NP surface is expected to occur mainly by the chemical bond between metal ions in the nanoparticle surface and the carboxyl groups of citric acid.<sup>39</sup> Following this procedure, we carried out several washing steps with deionized water and magnetic separation to remove the excess citric acid and residual salts. A colloidal dispersion of the NPs is obtained in pH 7, with the NPs surface in the anionic state which provides electrostatic repulsion.<sup>40</sup>

## 2.3 Structural and morphological characterization

We probed the chemical composition of the NPs using energy dispersive X-ray spectroscopy (EDX) with a Shimadzu EDX spectrometer. We measured the iron and manganese concentrations on the magnetic colloids with inductively coupled plasma optical emission spectroscopy (ICP-OES, Plasma Emission Spectrometer model OPTIMA 2100 DV, PerkinElmer, Waltham, MA, USA).

We checked the crystalline structure of the synthesized NPs by X-ray powder diffraction (XRPD) after air-dried evaporation of the liquid phase of the ferrofluid samples ( $80^\circ\text{C}$ ). Measurements were conducted with a Seifert XRD 3000 T/T diffractometer (Rich. Seifert & Co., Ahrensburg, Germany) using a Mo emitter ( $K\alpha$ :  $\lambda_1 = 0.0709316\text{ nm}$  and  $\lambda_2 = 0.0713607\text{ nm}$ ) and with  $2\theta$  ranging from  $7^\circ$  to  $57^\circ$ . The intrinsic width was measured using a  $\text{LaB}_6$  bulk sample (SRM 660 NIST). We conducted thermogravimetric analysis (TGA) to investigate the citric acid covering the NP surface. Measurements were taken in a Seiko (TG/DTA EXSTAR 6000 thermobalance). Samples were heated from  $25^\circ\text{C}$  to  $900^\circ\text{C}$  at  $5^\circ\text{C min}^{-1}$  in airflow.

The size distribution of the NPs was investigated by transmission electron microscopy (TEM) measurements using a 200 keV JEOL-2000FXII microscope. A diluted and sonicated ferrofluid drop was deposited on a carbon-coated copper grid. We

obtained size histograms by measuring approximately 1000 nanoparticles per sample using ImageJ software. The hydrodynamic diameter of the NPs was investigated by dynamic light scattering (DLS) measurements using a Zetasizer instrument (Malvern). Hydrodynamic volume and polydispersity index were estimated using a log-normal fitting of the DLS number distribution data.

## 2.4 Magnetic measurements

Magnetic measurements were made with a magnetometer based on a superconducting quantum interference device (MPMS-XL, Quantum Design) and a vibrating sample magnetometer (LDJ-9600, LDJ Electronics). We obtained hysteresis loops at ambient and low temperatures, 300 K and 5 K, after cooling in zero field. We measured the zero-field cooled (ZFC) and field-cooled (FC) magnetization curves as functions of temperature in a field of  $8\text{ kA m}^{-1}$  (100 Oe). The alternating-field magnetic susceptibility of the synthesized powders in toroidal sample holders was measured from 10 MHz to 1 GHz using an impedance analyzer (HP 4191A) with a GR900 adapter.<sup>41</sup>

## 2.5 Detection of magnetic nanoparticles

We studied the inductive detection performance of our NPs by using a radio-frequency inductive sensor designed for magnetic lateral flow strips.<sup>42</sup> The sensitive part of the sensor is a planar inductor, where an alternating current flows. A precision impedance analyser (Agilent 4294A) monitors the magnitude and phase of the coil's impedance using 16048 G test leads with a 500 mV excitation voltage that can operate at frequencies ranging between 20 MHz–110 MHz. A micro-positioner displaces the test strip (with a scanning length step  $\Delta l = 0.1\text{ mm}$ ) over the sensing inductor to detect the magnetic permeability variation of its environment. When the magnetic material approaches the inductor, the modification in magnetic permeability leads to a change in the impedance  $\Delta Z = Z - Z_0$  (where  $Z$  and  $Z_0$  are the measured impedance in the presence and absence of the magnetic nanoparticles, respectively). Such a modification depends on the initial magnetic susceptibility of the magnetic material as follows:<sup>42</sup>

$$\Delta Z(f, \chi', \chi'', \psi) = fL\psi\chi''(f) + ifL\psi\chi'(f), \quad (1)$$

where  $\chi'$  and  $\chi''$  are the real and imaginary components of the initial magnetic susceptibility, respectively,  $L$  the coil self-inductance, and  $\psi$  a proportionality factor ( $\psi < 1$ ) that accounts for the volume of particles. The real part of  $\Delta Z$  depends on the imaginary component of susceptibility  $\chi''$ , while the imaginary part of  $\Delta Z$  depends on the real part  $\chi'$  of susceptibility.

We investigated the inductive response of the synthesized NPs (before bioconjugation to NeutrAvidin) in the sensor by printing ferrofluids with different concentrations directly in the nitrocellulose (25 mm wide) with the backing card. Printing was made using an automatic micropipette coupled to a micro-positioner, programmed to dispense the ferrofluids across the membrane at a  $0.1\text{ }\mu\text{L mm}^{-1}$  rate. After drying, the



nitrocellulose containing the deposited NPs was cut into  $25 \times 7$  mm strips with a guillotine. We carried out five different depositions for each sample, with different ferrofluid concentrations, leading to different mass values of the deposited NPs. Our samples were measured using the same inductor and frequency (20 MHz) as in Salvador *et al.*,<sup>27</sup> to compare their performance with magnetite NPs.

We define the relative magnetic signal  $S$  as the relative increase of the impedance due to the contribution of all the deposited NPs:

$$K_{\text{eff}} \cong \frac{25 k_B \langle T_B \rangle}{\langle V \rangle}, \quad (2)$$

where  $\langle Z_0 \rangle$  is the mean value of the impedance in the absence of the NPs (base line). The integration is approximated by a sum over the number  $N$  of data points. The magnetic signal can also be expressed in absolute units of  $\Omega$  mm.

## 2.6 Lateral flow assays

**Strips preparation.** We prepared the lateral flow strips by attaching a nitrocellulose membrane (25 mm wide) to an adhesive backing plastic card. We printed the test line with a biotin-BSA solution ( $1000 \mu\text{g mL}^{-1}$ ) at a rate of  $0.1 \mu\text{L mm}^{-1}$  using the same automatic reagent dispenser described in the previous section. After 24 h for complete drying, we attached a glass fibre sample pad and an absorbent pad to the backing card at both sides of the membrane card, parallel to the printed line, with a 2 mm overlap with the nitrocellulose. Finally, we cut 5 mm individual wide strips using a guillotine.

**NP bioconjugation with NeutrAvidin and dipstick assays with biotin.** We bioconjugated the Mn-ferrite NPs with NeutrAvidin to perform lateral flow dipstick assays with a biotin-BSA test line, using the NeutrAvidin/biotin system as a dummy model of biorecognition. The idea is illustrated in Fig. 1A. This approach is widely used in immunoassay studies due to the high affinity and specificity of NeutrAvidin and biotin proteins.<sup>43</sup> In addition, several commercial proteins and antibodies are biotinylated, enabling a strong binding with NeutrAvidin.<sup>44,45</sup>

For the bioconjugation of the NPs with NeutrAvidin, first, 5  $\mu\text{L}$  of ferrofluid ( $6.7 \text{ mg mL}^{-1}$ ), previously sonicated for 5 minutes, was mixed with 10  $\mu\text{L}$  of EDC ( $1000 \mu\text{g mL}^{-1}$ ) freshly prepared in a phosphate-buffered saline solution (PBS 1 mM, pH 7.4). The mixture was placed in a vortex stirrer for 1 min. We added 100  $\mu\text{L}$  of a NeutrAvidin solution ( $1000 \mu\text{g mL}^{-1}$  in PBS 1 mM pH 7.4) to the mixture and put it in a refrigerated ultrasonic bath for different times: 1 min, 5 min, 10 min, 20 min, and 40 min. We repeated the same protocol without the EDC solution. We investigated different NeutrAvidin concentrations, ranging between  $0$ – $1000 \mu\text{g mL}^{-1}$ .

For this, we chose the optimized reaction time, *i.e.*, the bioconjugation protocol that led to the most intense test line.

For the LFAs, we mixed 20  $\mu\text{L}$  of freshly prepared NPs@NeutrAvidin conjugate with 80  $\mu\text{L}$  of a freshly prepared running buffer (RB) solution (10  $\text{mg mL}^{-1}$  BSA, 0.5% Tween20 in PBS 10 mM, pH 7.4). The assays were carried out by vertically

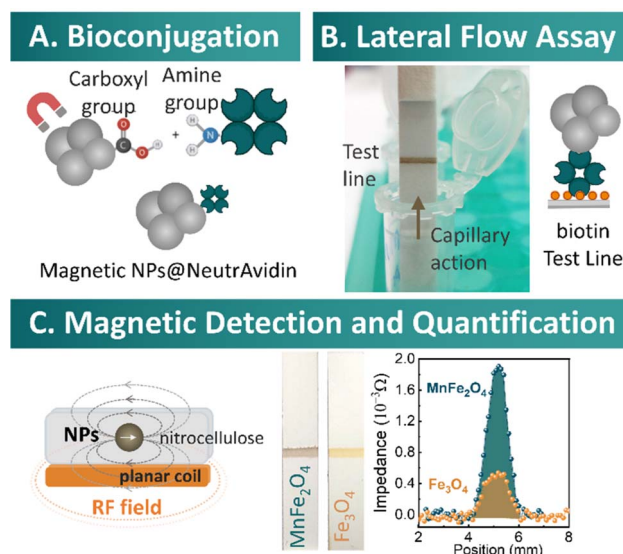


Fig. 1 (A) Scheme of NeutrAvidin bioconjugation with the NPs covered by free carboxyl groups. (B) Picture of a dipstick lateral flow strip printed with a biotin-BSA as a biorecognition element. The NPs@NeutrAvidin conjugate flows through the membrane and is retained in the biotin test line due to the strong NeutrAvidin/biotin affinity. The retained conjugates in the test line are seen thanks to the dark-brown color of the magnetic labels. (C) Scheme of the magnetic detection of the NPs in the nitrocellulose membrane by the radio-frequency inductive sensor (left). At right, typical curves from the test line of a magnetic LFA using the  $\text{MnFe}_2\text{O}_4$  nanoparticles of this work (dark-brown line) and  $\text{Fe}_3\text{O}_4$  nanoparticles covered by a double layer of oleic acid<sup>46</sup> (orange test line).

introducing the sample pad into an Eppendorf tube containing the RB and the NPs@NeutrAvidin conjugate (dipstick format), as illustrated in Fig. 1B. The magnetic nanolabels retained in the test line were detected and quantified by a radiofrequency inductive sensor, and the magnetic signal was analyzed to investigate the optimization of bioconjugation parameters. In addition, for the different NeutrAvidin concentrations, we measured the optical signal of the test line using a mobile telephone camera. We analyzed the gray value intensity profile using ImageJ software.<sup>7</sup> We compared the optical and magnetic signals of our labels. All assays were performed in triplicates.

## 3. Results and discussions

In lateral flow assays, a nanotag is used to mark the analyte of interest for detection. In the case of magnetic nanolabels, they can be detected and quantified not only by the naked eye but also by magnetic readers. The inductive sensor we used, specially developed for reading LFAs,<sup>24</sup> is based on magnetic induction and depends on the initial magnetic susceptibility of the magnetic nanotags. We prepared Mn ferrite nanoparticles in this work because their bulk counterparts have low magnetocrystalline anisotropy, which result in a high initial susceptibility and a high detection signal in inductive sensors. We synthesized two samples with different mean diameters and characterized their properties to correlate with their signal in





the inductive sensor. We tested the viability of these NPs as nanotags in lateral flow dipstick assays using the NeutrAvidin/biotin system.

### 3.1. Physicochemical characterization of the NPs

The stoichiometric  $\text{MnFe}_2\text{O}_4$  composition of the particles was obtained by fixing the precursors  $\text{Mn}^{2+}:\text{Fe}^{3+}$  volumetric proportion to 1:2. The stoichiometry was confirmed by EDX measurements, yielding a Mn fraction  $x_{\text{Mn}} = [\text{Mn}]/([\text{Mn}] + [\text{Fe}])$  of 0.33, as expected. However, the ICP composition measured in the final colloidal dispersions (after the functionalization with citric acid) had a proportion of  $x_{\text{Mn}} = 0.26$  for both samples. This is a consequence of the  $\text{Mn}^{2+}$  release from the NP surface in acidic media.<sup>47</sup> Similar results have been reported with other acidic surface treatment,<sup>30,48</sup> including other doped-ferrites.<sup>49</sup> The acid attack is stronger for the  $\text{Mn}^{2+}$  cations than for the  $\text{Fe}^{3+}$  cations, which are more chemically stable in acid media,<sup>30</sup> and it produces a thin  $\text{Fe}^{3+}$ -rich layer at the NP surface, giving rise to a core-shell-like chemical structure. We accounted for such findings to determine the NP concentration of the final colloidal dispersions using a core-shell model of chemical composition.<sup>48,49</sup>

The TG/DTA measurements shown in Fig. 2A investigated the citric acid coating. From TG curves, a slight loss in mass occurs at low temperatures (until 100 °C), with an endothermic peak in DTA related to the desorption of absorbed water onto the NP surface. This is followed by a significant mass loss above

160 °C, with an exothermic peak at  $\sim 230$  °C. This is expected for the decomposition and removal of the citric acid molecules chemically attached to the NP surface.<sup>50</sup> We obtained a higher mass loss for the S2 sample in this temperature range, likely due to a larger amount of citric acid. In addition, a secondary weight loss with an exothermic peak occurs at  $\sim 300$  °C, mainly for S2 sample, which would be related to a double layer of citric acid, one stronger bonded to NPs than the second one, as reported for citric acid coated magnetite NPs.<sup>51</sup> Such results confirm the success of citric acid coating and the availability of carboxyl –COOH reactive groups for bioconjugation. Near pH 7, –COOH undergoes deprotonation, leading to carboxylate –COO<sup>−</sup> anions at the NP surface.<sup>51</sup> This provides additional electrostatic repulsion among the NPs, essential for colloidal stability. Following the more significant mass decrease in both samples until  $\sim 300$  °C, two minor bumps with mass growth appear in TG curves. Given that the experiments were conducted in an airflow atmosphere, these measurements are probably associated with the oxidation process of  $\text{Mn}^{2+}$  to  $\text{Mn}^{3+}$  and  $\text{Mn}^{3+}$  to  $\text{Mn}^{4+}$  at higher temperatures. This seems more pronounced for the S1 sample, which has a smaller citric acid content (7.5%) than S2 (11.6%) and a higher surface area due to its smaller mean diameter, as it will be shown later by TEM measurements (8 nm vs. 10 nm).

### 3.2. Structural and morphological characterization

The X-ray powder diffractograms of the two synthesized NPs (Fig. 2B) have characteristic diffraction lines from a single crystalline spinel structure. This pattern closely matches the bulk standard data from the International Centre for Diffraction Data (ICDD) for bulk  $\text{MnFe}_2\text{O}_4$  (ICDD 01-073-1964). No additional lines were apparent in the diffractogram, confirming the absence of any byproduct, such as other Mn- or Fe-oxides, and the purity of the synthesized material. We analyzed the spectra by fitting a pseudo-Voigt function to obtain the peaks' position and breadth (the intrinsic beam width was discounted using a  $\text{LaB}_6$  standard). The crystalline diameters of the NPs were obtained using Scherrer's formula,  $D_{\text{XRPD}} = 0.9 \lambda / \beta \cos \theta$ , with  $\beta$  being the width at half-maximum of the peak. We considered as the crystallite diameter the average between the peaks of the XRPD spectra; Table 1 summarizes the results. Increasing the stirring rate in the coprecipitation leads to a reduction in the crystalline diameter from 9.4 nm to 7.7 nm. This finding corroborates previously published work with other ferrites.<sup>37,52,53</sup> It can be associated with an increasing diffusion of the precursor species, which may promote the fast formation of several nuclei at the expense of crystalline growth.

We have determined the lattice parameter  $a$  from Bragg's law  $n\lambda = 2d_{hkl}\sin\theta$ , with  $d_{hkl}$  being the interplanar distances of the  $\{hkl\}$  family planes ( $h$ ,  $k$  and  $l$  being the Miller indices) and  $n$  the order of diffraction. We also considered the cubic symmetry of the spinel structure, where  $d_{hkl} = a/(h^2 + k^2 + l^2)^{1/2}$ . We determined  $a$  for all peaks and calculated the average of them. Results are also shown in Table 1; for the two samples, the values are very close to those of Mn-bulk ferrite<sup>28</sup> (0.850 nm). We estimated the density of the NPs considering the volume

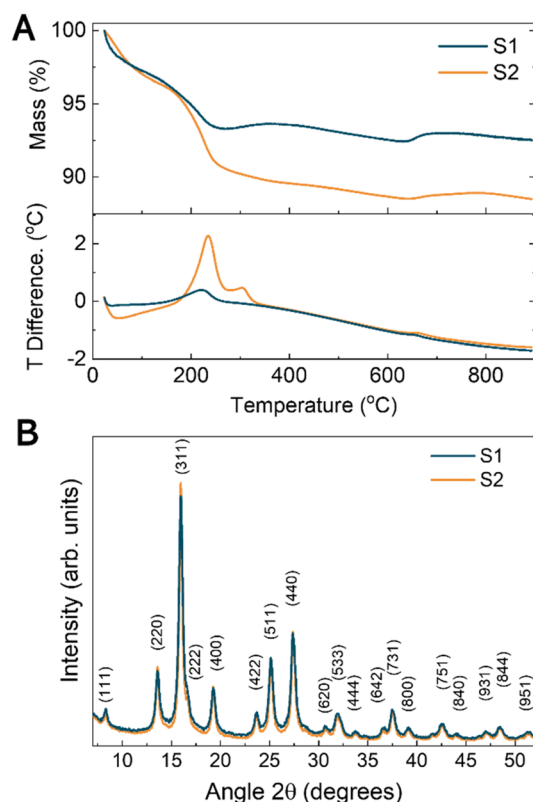


Fig. 2 (A) TG/DTA measurements of the two synthesized samples. (B) XRPD diffractogram of the two samples.



**Table 1** Sample characteristics as a function of stirring rates used in the coprecipitation reaction;  $D_{\text{XRPD}}$  is the crystallite diameter and  $a$  is the lattice parameter, both obtained from XRPD measurements.  $D_0^{\text{TEM}}$  and  $\sigma^{\text{TEM}}$  are the characteristic diameter and polydispersity index obtained from TEM measurements, respectively.  $D_0^{\text{DLS}}$  and  $\sigma^{\text{DLS}}$  are the hydrodynamic mean diameter and the polydispersity index from the DLS measurements

Sample	Stirring rate (rpm)	$D_{\text{XRPD}}$ (nm)	$\langle a \rangle$ (nm)	$D_0^{\text{TEM}}$ (nm)	$\sigma^{\text{TEM}}$	$D_0^{\text{DLS}}$ (nm)	$\sigma^{\text{DLS}}$
S1	360	7.7	0.849	8	0.34	27	0.26
S2	170	9.4	0.849	10	0.25	29	0.20

occupied by the cubic cell ( $a^3$ ) and the atomic mass inside it.<sup>48</sup> Hence, we obtained  $5008 \text{ kg m}^{-3}$  for the two samples, fairly close to that of bulk ferrite<sup>28</sup> ( $4990 \text{ kg m}^{-3}$ ).

Fig. 3A and B are TEM micrographs of the two samples. The NPs are quasi-spherical in both samples. The size-distribution histogram (Fig. 3E) fits well to a log-normal probability function – the best fitting yields the values in Table 1 for the characteristic size and polydispersity. The sample synthesized at a low stirring rate (S2) has the largest particles and a narrower size distribution.

We estimated the two samples' hydrodynamic diameter and polydispersity index by DLS measurements (Fig. 3F and Table 1). The resulting values are 27 and 29 nm with PDIs around 25%, which are slightly larger than the TEM sizes, indicating some NP clustering ( $\sim 2$ – $5$  NPs per cluster). Indeed, DLS results are compatible with the small NP assemblies in the TEM micrographs of significantly diluted and sonicated samples (Fig. 3C and D). Aggregation is undesirable for many NP bio-applications because it can compromise the performance of magnetic nanoparticles (for magnetic imaging or drug delivery,

for example) and even lead to significant challenges in *in vivo* applications (vascular risks associated with clot formation). However, for *in vitro* magnetic detection in LFA, it can be beneficial. Some agglomeration (as long as the agglomerates can flow through the membrane pores) can enhance the detection sensitivity for quantification because it increases the number of NPs and magnetic signal per biomolecule.<sup>7,46</sup>

### 3.3 Magnetic properties

Fig. 4A shows the hysteresis loops for both samples at 300 K and 5 K. The inset provides a close-up of the central region. At 300 K, it shows non-zero coercivity, although less than  $1.0 \text{ kA m}^{-1}$ . This is attributable to a small fraction of large NPs in a blocked regime. At 5 K all the particles are blocked, producing an increase of coercivity up to  $11.6 \text{ kA m}^{-1}$ . The specific saturation magnetization  $M_s$  was obtained by fitting the experimental data to LAS, the law of approach to saturation<sup>54</sup>  $M(H) = M_s (1 - a_1/H - a_2/H^2) + a_3H$ , where the fitting parameters are:  $a_1$  related to structural defects,  $a_2$  to the magnetocrystalline and shape

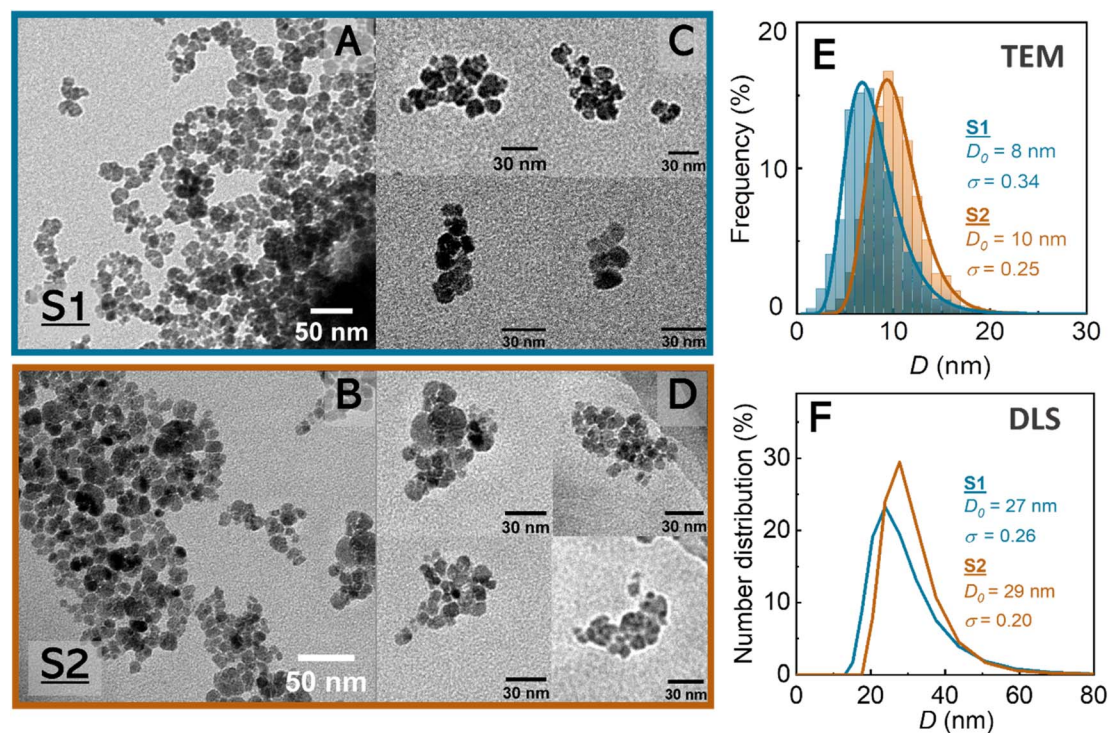


**Fig. 3** (A and B) TEM micrographs of S1 and S2 samples. (C and D) Regions of some TEM micrographs of significantly diluted and sonicated samples, suggesting the presence of small NP aggregates in the samples. (E) Size distribution histograms of approximately 1000 NPs with a log-normal distribution fitting. (F) Hydrodynamic size distributions of the two samples.



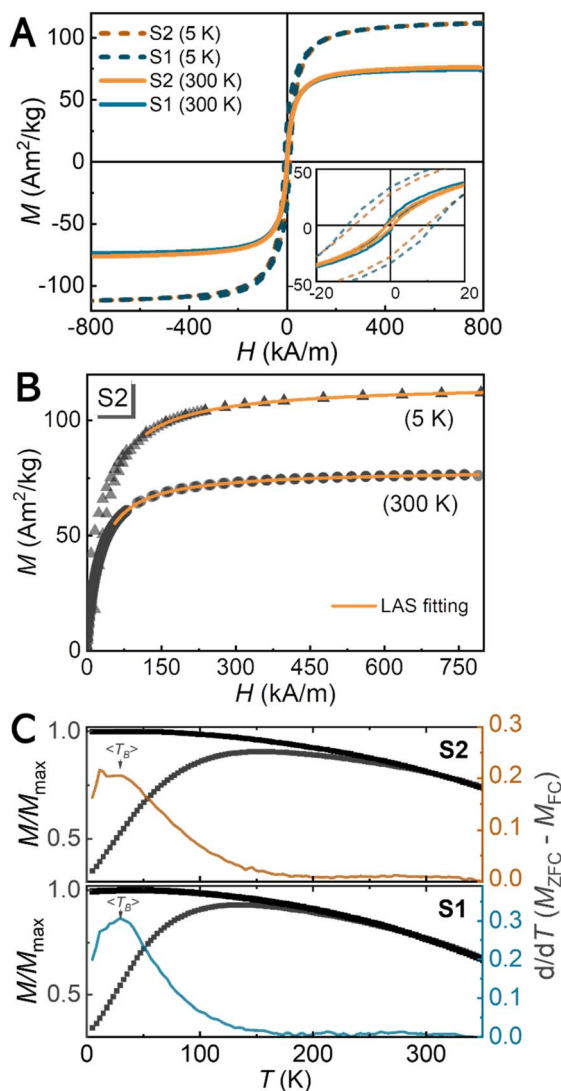


Fig. 4 (A) Hysteresis loops at room and low temperatures of the two synthesized samples. The inset shows an enlarged view of the hysteresis loops. (B) Determination of the specific saturation magnetization using LAS at room and low-temperature measurements, respectively, for a representative sample. (C) ZFC and FC curves (with a 100 Oe FC) of the two samples and determination of mean blocking temperature.

anisotropies<sup>54</sup> and  $a_3$  is resulting from the high-field susceptibility.<sup>55</sup> It is important to mention that the magnetization curves were performed in powder samples, where magneto-dipole interactions should be present. In such a scenario, LAS is a suitable approach to fit  $M(H)$  curves. Results are found in Fig. 4 and Table 2 and LAS fitting parameters are in Table ESI 1.† The two samples have a high  $M_s$ , close to those for bulk Mn-ferrite.<sup>28</sup> The reduced remanence  $M_R/M_s$  of the low-temperature hysteresis loops are 0.3 (S1) and 0.2 (S2), both lower than 0.5, the value predicted by the Stoner–Wohlfarth model<sup>56</sup> for randomly oriented monodomain ferromagnetic nanoparticles with uniaxial magnetic anisotropy in a non-interacting regime. This would be attributed to an additional source of magnetic anisotropy.

In nanoscale, a surface of disordered spins induced by the reduced coordination at the nanoparticle surface increases the low-temperature saturation magnetization,<sup>57</sup> therefore reducing the expected squareness  $M_R/M_s$  at low temperatures. However, this surface effect is more pronounced for ultrasmall NPs ( $\sim 3$  nm).<sup>57</sup> The  $M_s$  values for both our samples are very close to the bulk Mn-ferrite, suggesting a very small surface effect on low-temperature magnetization. Indeed, the NP magnetic cores estimated by fitting the Langevin–Chantrell approximation<sup>58</sup> to the room temperature data are 7 nm and 9 nm for S1 and S2 NPs, respectively, very close to TEM values. Since measurements were conducted in powder, we associate the decrease in the reduced remanent magnetization mainly to magnetic dipolar interactions, which can produce a demagnetizing effect on the system's remanence.<sup>59,60</sup> Further investigations on the nature and intensity of the magnetic interactions would provide valuable insights into clarifying this issue.

We evaluated the magnetic anisotropy of our samples through the blocking temperature. The blocking temperature characterizes the transition from a (i) blocked regime, when the magnetic moments are frozen in the easy magnetization axis (pointing to one of the possible directions), to a (ii) superparamagnetic (SPM) regime, when the magnetic moment has enough thermal energy to flip from one direction to the other during the measuring time.

The transition between the two regimes depends on the NP volume, magnetic anisotropy, measuring time, and magnetic field strength. We measured the ZFC-FC curves to investigate the blocking temperatures, as illustrated in Fig. 4C. In monodisperse systems, the blocking temperature corresponds simultaneously to the peak of the ZFC curves and the point where the ZFC and FC curves intersect. However, for poly-disperse NPs, these temperatures are notably distinct. When there is a volume distribution, there will be a distribution of blocking temperatures. Therefore, the broader distribution, the wider transition range between blocked to SPM regimes.

The distribution of blocking temperatures was investigated by calculating the derivative of the difference between ZFC and FC curves.<sup>61,62</sup> The mean blocking temperatures  $T_B$  are indicated in Fig. 4C and their values reported in Table 2. A secondary peak is evident in the derivative curve at  $T = 12$  K for both samples, more pronounced for S2. Since NPs have a well-fitted log-normal size distribution, the presence of a secondary peak in the derivative curve could be related to a superspin glass state at low temperature<sup>63,64</sup> due to strong dipolar interactions.<sup>65</sup> We estimated the effective anisotropy constant  $K_{\text{eff}}$  values for both samples by considering the values in Table 2 and using the following equation:<sup>66</sup>

$$K_{\text{eff}} \cong \frac{25 k_B T_B}{V}, \quad (3)$$

where  $k_B$  is the Boltzmann constant and  $V$  is the characteristic NP volume. We also determined the room-temperature  $K_{\text{eff}}$  values using the  $a_2$  parameter from LAS fitting to 300 K magnetization data (Table S1 of ESI†) and assuming  $K_{\text{eff}} = \mu_0 M_s (15a_2/4)^{1/2}$  for uniaxial anisotropy,<sup>55</sup> where  $\mu_0$  is the vacuum magnetic permeability. Results are found in Table 2; in both





**Table 2** Magnetic properties of the synthesized samples: specific saturation magnetization at ambient temperature and low temperature, coercive field at low temperature, mean blocking temperature, effective magnetic anisotropy obtained from ZFC/FC curves and from LAS fitting (300 K), respectively, and initial magnetic susceptibility at ambient temperature and 20 MHz (in-phase and out-of-phase components and modulus)

Sample	$M_s^{(300\text{ K})}$ ( $\text{A m}^2 \text{ kg}^{-1}$ )	$M_s^{(5\text{ K})}$ ( $\text{A m}^2 \text{ kg}^{-1}$ )	$H_c^{(5\text{ K})}$ ( $\text{kA m}^{-1}$ )	$\langle T_B \rangle$ (K)	$K_{\text{eff}}^{\text{ZFC/FC}}$ ( $10^4 \text{ J m}^{-3}$ )	$K_{\text{eff}}^{\text{LAS (300 K)}}$ ( $10^4 \text{ J m}^{-3}$ )	$\chi'$	$\chi''$	$ \chi $
S1	76.3	115.2	11.6	29	3.8	1.4	12.8	4.1	13.4
S2	78.2	115.3	9.8	30	1.8	1.5	13.8	3.8	14.3

cases  $K_{\text{eff}}$  values are one order of magnitude larger than the bulk Mn ferrite value<sup>28</sup> ( $0.3 \times 10^4 \text{ J m}^{-3}$ ). This would be due to additional contributions to the effective magnetic anisotropy, such as a surface-induced contribution due to a disordered spin shell at the nanoparticle surface,<sup>57,67</sup> dipolar interactions,<sup>68</sup> and shape contributions.

To go further in understanding the very small coercivity observed at room temperature, we estimated the critical diameter for superparamagnetic behaviour at room temperature by assuming  $T = 300 \text{ K}$  in the expression  $D_C(T) = (150 k_B T / \pi K_{\text{eff}})^{1/3}$ . We found that for both S1 and S2 samples, NPs larger than 24 nm are blocked at room temperature. Such sizes correspond to less than 0.1% of S2 NPs and 1.2% of S1 NPs. These estimations suggest that most NPs of the size distribution are in a superparamagnetic regime at room temperature.

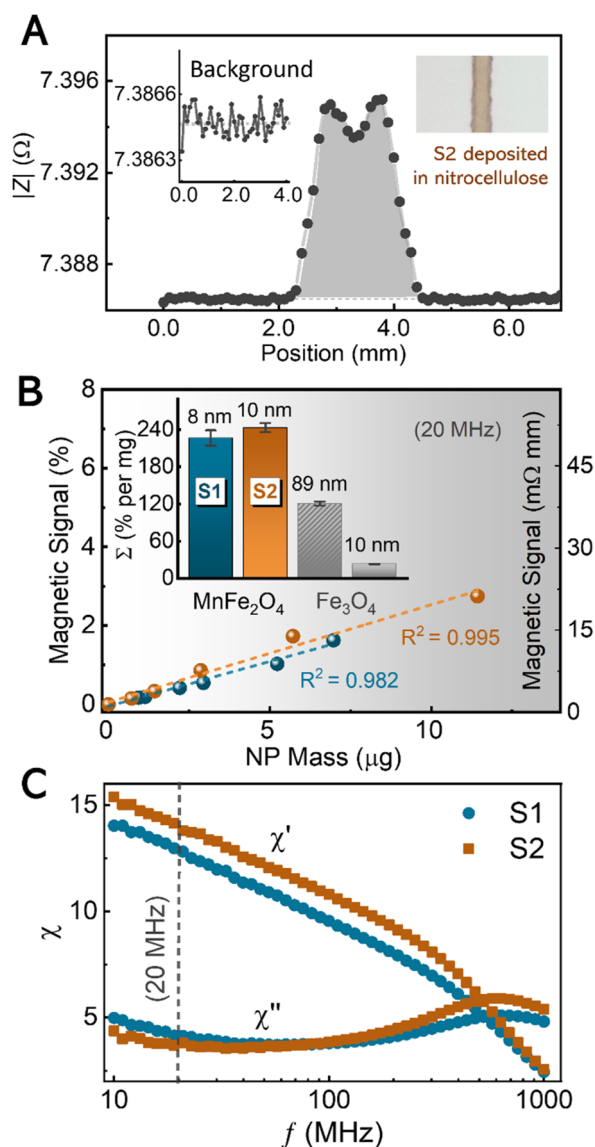
### 3.4. Inductive response of the NPs in the sensor

Fig. 5A illustrates a typical measurement of a printed ferrofluid in the nitrocellulose membrane using the inductive sensor. The inset shows a “coffee ring effect” obtained after the aqueous phase of the printed colloid evaporates. The “coffee ring” is a spontaneous phenomenon for any aqueous colloidal dispersion of nanoparticles. After the colloid is deposited on a flat surface, or in this case, a porous membrane surface, the water evaporates faster from the edges, and the rest of the colloid moves to take its place, producing the pattern.<sup>69,70</sup>

Measurement is carried out after drying for 24 h. The term “magnetic signal” refers to the relative increase of the impedance due to the contribution of all the deposited NPs (see the highlighted area in Fig. 5A). It is calculated using eqn (2) and considering the modulus of the complex impedance  $|Z|$ . We deposited the ferrofluid samples (before bioconjugation) with different concentrations onto the nitrocellulose membrane and measured their sensor signal as a function of NP mass. Results are presented in Fig. 5B. We obtained a linear trend for this range of NP mass, which agrees with previous studies with the same sensor.<sup>42</sup> The slope of the best-fitted straight line corresponds to the sensor sensitivity, which is the relative increase of the impedance per unit mass of NPs as follows:

$$\Sigma = \frac{S}{m} \cong \frac{1}{m} \sum_{i=1}^N \left( \frac{Z_i - Z_{0i}}{Z_{0i}} \right) \times 100. \quad (4)$$

The obtained values are shown on the inset of Fig. 5B: 226% per mg of S1 NPs and 243% per mg of S2 NPs. The slightly superior performance of S2 NPs compared to the S1 NPs can be



**Fig. 5** (A) Typical measurement of a line of ferrofluid sample deposited onto the nitrocellulose membrane, measured by the inductive magnetic sensor. On the inset: nitrocellulose and backing card measurement, without deposited NPs (left) and “coffee-ring” pattern (right). (B) Magnetic sensor signal as a function of the deposited NP mass. The inset shows the sensor sensitivity using our  $\text{MnFe}_2\text{O}_4$  NPs and previous results with 89 nm highly dense  $\text{Fe}_3\text{O}_4$  nanoclusters (gray striped bar)<sup>7</sup> and 10 nm coprecipitated  $\text{Fe}_3\text{O}_4$  NPs (gray bar).<sup>46</sup> (C) AC initial magnetic susceptibility measured at high frequencies. Both real and imaginary components are shown for the two samples.





attributed to the higher NP mean diameter, which can produce a higher magnetic initial susceptibility. Both values are higher than the obtained ones for magnetite measured with the same sensor: 23% per mg of 10 nm coprecipitated Fe<sub>3</sub>O<sub>4</sub> NPs covered by a double layer of oleic acid<sup>46</sup> and 121%/mg of magnetite nanoclusters coated with polyacrylic acid (PAA).<sup>7</sup> We also determined the resolution, which is the minimum mass that can be detectable by the sensor, given by

$$R = 3\sigma_{\text{Noise}}N/\Sigma, \quad (5)$$

where  $\sigma_{\text{Noise}}$  is the noise standard deviation of background and  $N$  is the number of data points. We obtained a resolution of only 0.72 ng for S2 NPs and 0.87 ng for S1 NPs, outperforming our previous best result of 1.6 ng for magnetite nanoclusters.<sup>7</sup> These findings suggest that superparamagnetic Mn-ferrite nanoparticles are more sensitive than magnetite for magnetic detection in inductive sensors.

We measured the frequency dependence of the complex initial magnetic susceptibility  $\chi = \chi' - i\chi''$  in high frequency. The real part is proportional to the induced in-phase magnetization, while the imaginary part is proportional to the out-of-phase magnetization (magnetic losses). Results are shown in Fig. 5C.

The dashed line in Fig. 5C highlights the frequency of 20 MHz, which was the same used for the measurements in the magnetic sensor, providing a good signal-to-noise ratio. The real part of the susceptibility  $\chi'$  is slightly higher for S2 NPs. Regarding the imaginary part ( $\chi''$ ), there are similarities between the two samples, including a presumed resonance frequency of 630 MHz. The higher susceptibility for S2 samples is likely related to the larger mean NP diameter. Nonetheless, the values for the two components of initial magnetic susceptibility (see Table 2) are an estimate because the measurements were made on powders, where the magnetostatic interactions among the particles are strong and would reduce the intrinsic initial magnetic susceptibility.<sup>71</sup> The resonance peaks in the imaginary part are expected to occur when  $2\pi f\tau = 1$ ,  $\tau$  being only the Néel relaxation  $\tau = \tau_0 \exp(K_{\text{eff}}V/k_{\text{B}}T)$ , since particles cannot move, and  $\tau_0$  the spin relaxation time. We estimated the effective anisotropy constant value by assuming the resonance frequency  $f = 630$  MHz and  $\tau_0 = 10^{-10}$  s. The results for S1 and S2 samples are  $1.4 \times 10^4$  J m<sup>-3</sup> and  $0.7 \times 10^4$  J m<sup>-3</sup>, respectively, both are very close to those presented in Table 2, which were obtained by LAS fitting to the 300 K data.

### 3.5. Lateral flow dipstick assays and magnetic quantification

We investigated S2 citrate-coated MnFe<sub>2</sub>O<sub>4</sub> NPs as detection nanolabels in LFAs using the NeutrAvidin/biotin model of bio-recognition. In these experiments, the NeutrAvidin protein plays the role of target-molecule. Before the bioconjugation, the protein was diluted in PBS (1 mM pH 7.4) at different concentrations to obtain ten biological samples. The protein was conjugated to the S2 NPs to be detectable. To retain them in a dipstick assay, the nitrocellulose membrane strips had a line of biotin-BSA (1000 µg mL<sup>-1</sup>) printed across them.

The biological fluids were tested with the LFA; in all of them, the proteins labelled with magnetic NPs were retained at the biotin line, forming a visible test line (see the upper part of Fig. 6C). The lines were quantified using a radiofrequency inductive sensor and a mobile telephone camera.

We started with a high concentration of NeutrAvidin (1000 µg mL<sup>-1</sup>) to test the bioconjugation protocol immediately after different reaction times in a refrigerated ultrasonic bath. Results are shown in Fig. 6A. The magnetic signal is proportional to the number of nanolabels retained in the test line, which depends on the amount of NeutrAvidin tagged with NPs. We obtained a fast bond between the citrate-coated S2 NPs and the NeutrAvidin protein. For the EDC-mediated reaction (gray bars in Fig. 6A), we observed a high signal after 1 min, which decreased with sonication time. Without using the EDC cross-linker (orange bars in Fig. 6A), we achieved an optimized signal after 5 and 10 min of sonication. We kept these two optimized conjugates resting for 150 min without sonication and we repeated the assays, obtaining a reproducible magnetic signal at test line, as shown in the inset of Fig. 6A. This suggests that NPs@NeutrAvidin bonding occurs fast and is stable at rest using the present protocol. However, a reduction in test line signal occurs when increasing sonication time, suggesting a partial rupture of the S2-NeutrAvidin conjugate, likely related to the NeutrAvidin desorption from the NP surface.

Fig. 6B depicts the magnetic and optical signal as a function of NeutrAvidin concentration (8–1000 µg mL<sup>-1</sup>). For such an investigation, we chose the optimized sonication time of 5 min without EDC chemistry. We also checked the specificity of the NeutrAvidin/biotin biorecognition in our LFA by using the same protocol, however, without NeutrAvidin (blank control sample). The test lines of our LFAs are shown in the upper part of Fig. 6B. No signal was obtained for the blank sample, confirming the specificity of the assays. The magnetic signal increases with increasing NeutrAvidin concentration until a saturated value of  $\sim 1700$  µΩ mm above 250 µg mL<sup>-1</sup> of NeutrAvidin, corresponding to  $\sim 949$  ng of S2 NPs retained in the test line. The trend is linear for the range of NeutrAvidin concentrations until  $\sim 31$  µg mL<sup>-1</sup>, as seen on the inset of Fig. 6B, together with the fitting parameters, corresponding to 474 ng of S2 NPs in the test line. For the smaller NeutrAvidin concentration we tested (8 µg mL<sup>-1</sup>), we found 133 ng of NPs in the test line.

The optical signal obtained with a mobile telephone camera had very similar behavior. We got a better coefficient of determination  $R^2$  and lower standard deviation with the magnetic measurements than with the optical data. This is mainly related to variations in optical signal because of different ambient light.

The hydrodynamic diameters obtained by DLS (see Fig. 6C) increased from 29 nm (before bioconjugation) to 38 nm (after 1 min of NeutrAvidin bioconjugation). This difference corroborates the bioconjugation with NeutrAvidin, which has a diameter of 4–5 nm (60 kDa),<sup>72,73</sup> and the absence of a significant post-bioconjugation clustering.

The magnetic signal obtained for our 10 nm MnFe<sub>2</sub>O<sub>4</sub> NPs (S2) bioconjugated with NeutrAvidin (1000 µg mL<sup>-1</sup>) outperformed previously published results with different Fe<sub>3</sub>O<sub>4</sub> NPs with the same NeutrAvidin concentration and measured with the same



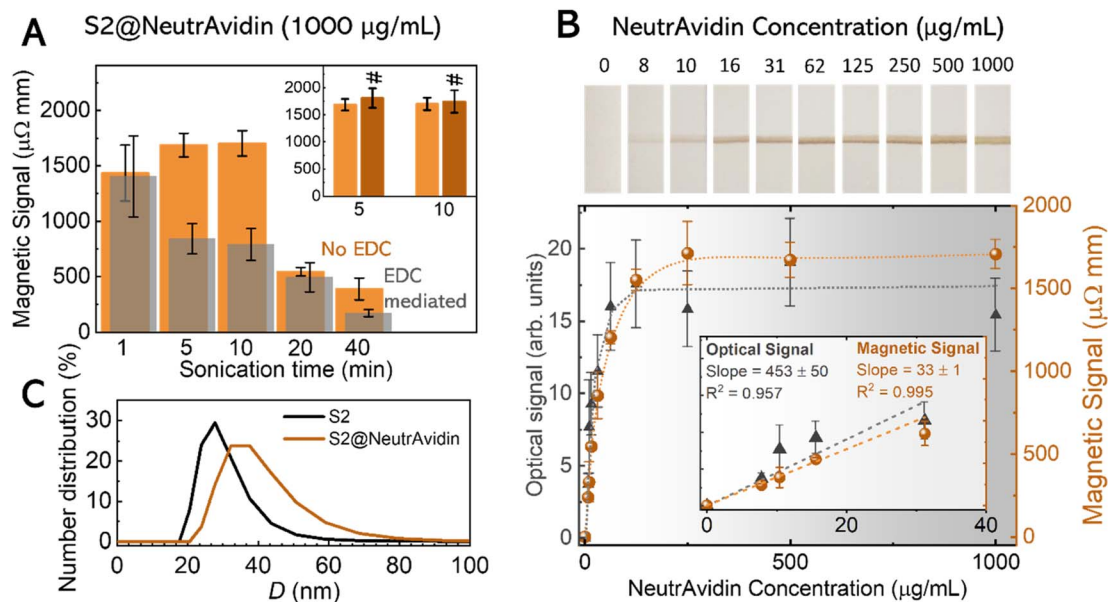


**Fig. 6** (A) Magnetic signal obtained for biotin-BSA test line after NPs@NeutrAvidin bioconjugation with different sonication times. Gray bars are related to the EDC-mediated protocol, and orange bars were obtained without EDC chemistry. The inset shows the optimized sonication times (5 and 10 min) and repeated assays after 150 min with the sample kept at rest (without sonication – marked with # symbols). (B) Magnetic and optical signal for different NeutrAvidin concentrations. In the upper part, we see the modifications in the strip's test line intensities. The inset depicts the linear dependency of magnetic and optical signals for the smallest NeutrAvidin concentrations tested. (C) DLS number distribution before and after 1 min bioconjugation (black and orange, respectively).

sensor and frequency: 573  $\mu\Omega$  mm for 10 nm NPs covered with oleic acid, 630  $\mu\Omega$  mm for 7.9 nm lauric acid-coated NPs and 1250  $\mu\Omega$  mm for 9.5 nm NPs covered with myristic acid.<sup>46</sup> Also, we achieved similar values to the reported one for 89 nm  $\text{Fe}_3\text{O}_4$  nanoclusters covered with polyacrylic acid.<sup>7</sup> Since S2 NPs are smaller, this may be attributed to the heightened sensitivity of  $\text{MnFe}_2\text{O}_4$  NPs for detection in inductive sensors.

The fast binding of NeutrAvidin to the NPs in the bioconjugation protocols we tested probably occurred due to an electrostatic union between negative ions on the NP surface and positive charges of the NeutrAvidin in PBS (1 mM, pH 7.4), expected because of its isoelectric point<sup>74</sup> of 6.3. Indeed, chemical bonding between proteins and the nanoparticle surface may occur in several ways, including electrostatic union between negative charges on the NP surface and positive charges in the protein and covalent binding between carboxyl on the NP surface and amines in the protein, among others.<sup>75</sup> The latter is generally intermediated by the EDC/NHS chemistry<sup>76</sup> and occurs slowly, but is generally preferred in immunoassays due to its greater stability. Therefore, for future development of real immunoassays, the bioconjugation protocol must be optimized considering the biomarkers of interest for a specific immunoassay architecture.

## 4. Conclusions

We synthesized two samples based on Mn-ferrite nanoparticles using the hydrothermal coprecipitation technique and a functionalization protocol with citric acid. We investigated their physico-chemical and magnetic properties, as well as their performance for magnetic detection and for the development of lateral flow assays. The sample obtained with the slowest stirring rate (S2) during the

coprecipitation reaction had a larger mean diameter, lower polydispersity, and a smaller fraction of blocked NPs at room temperature. This sample had the higher initial magnetic susceptibility at the megahertz frequency range and showed a greater sensitivity for magnetic detection in our magnetic sensor at a frequency of 20 MHz. The Mn-ferrite NPs of this work provided considerably higher sensor sensitivity and lower resolution compared with previously published work with magnetite NPs.

We further investigated the use of 10 nm S2 NPs as magnetic tags in LFAs using the NeutrAvidin/Biotin model of bio-recognition. In our protocol, we achieved an intense signal on the test line just after 5 min of bioconjugation without employing EDC chemistry, suggesting an electrostatic bonding between the NP surface and the NeutrAvidin. The magnetic signal obtained for the 1 mg mL<sup>-1</sup> of NeutrAvidin was compared to that obtained for magnetite nanoclusters on our inductive sensor. Our findings suggest that  $\text{MnFe}_2\text{O}_4$  nanoparticles and their assemblies have strong potential for further development magnetic lateral flow immunoassays for biomarkers detection and sensitive magnetic quantification.

## Data availability

Data are available from the corresponding author on request.

## Author contributions

VP: conceptualization, investigation, methodology, writing – original draft and visualization; MS: data curation, visualization, methodology, writing – review & editing; LBF: data curation and validation; JLMF: data curation and validation; FGS:



writing – review & editing, validation; MF: data curation; RLA: data curation, resources, writing – review & editing; MPM: resources, writing – review & editing; JCMG: conceptualization, resources, writing – review & editing; MR: conceptualization, formal analysis, writing – review & editing, resources and funding acquisition.

## Conflicts of interest

There are no conflicts to declare.

## Acknowledgements

The authors acknowledge financial support from the Ministry of Science and Innovation of the Spanish Government under grant PLEC2022-009490, the University Technological Institute of Asturias (IUTA) under grant SV-22-GIJON-18, the Government of the Principality of Asturias under projects FICYT/IDI/2021/000100 and FICYT/IDI/2021/00027, the Brazilian agency Federal District Research Support Foundation (FAPDF), under grant 00193-00001862/2023-06, and the Plan Propio de la Universidad de Castilla-La Mancha (FEDER, EU) 2022-GRIN-34313. Technical support was provided by Graciela Castellanos and the technical service of the University of Oviedo and the Instituto de Ciencia de Materiales de Madrid. Ron Goldfarb, NIST, contributed the susceptibility measurements in Fig. 5C and helpful comments on the manuscript. M.S. was supported by a Margarita Salas fellowship financed by the European Union-Next Generation EU and the Plan for Recovery, Transformation, and Resilience. Some of the figures in this article were created with <https://www.biorender.com/>.

## References

- 1 Y. Liu, L. Zhan, Z. Qin, J. Sackrison and J. C. Bischof, *ACS Nano*, 2021, **15**, 3593–3611.
- 2 D. Quesada-González, G. A. Jairo, R. C. Blake, D. A. Blake and A. Merkoçi, *Sci. Rep.*, 2018, **8**, 16157.
- 3 N. Mandal, S. Mitra and D. Bandyopadhyay, *IEEE Sens. J.*, 2019, **19**, 7936–7941.
- 4 X. Huang, Z. P. Aguilar, H. Xu, W. Lai and Y. Xiong, *Biosens. Bioelectron.*, 2016, **75**, 166–180.
- 5 A. Sharma, A. I. Y. Tok, C. Lee, R. Ganapathy, P. Alagappan and B. Liedberg, *Sens. Actuators, B*, 2019, **285**, 431–437.
- 6 Z. Bai, H. Wei, X. Yang, Y. Zhu, Y. Peng, J. Yang, C. Wang, Z. Rong and S. Wang, *Sens. Actuators, B*, 2020, **325**, 128780.
- 7 M. Salvador, J. L. Marqués-Fernández, A. Bunge, J. C. Martínez-García, R. Turcu, D. Peddis, M. D. M. García-Suárez, M. D. Cima-Cabal and M. Rivas, *Nanomaterials*, 2022, **12**, 2044.
- 8 D.-B. Wang, B. Tian, Z.-P. Zhang, X.-Y. Wang, J. Fleming, L.-J. Bi, R.-F. Yang and X.-E. Zhang, *Biosens. Bioelectron.*, 2015, **67**, 608–614.
- 9 F. Liu, H. Zhang, Z. Wu, H. Dong, L. Zhou, D. Yang, Y. Ge, C. Jia, H. Liu, Q. Jin, J. Zhao, Q. Zhang and H. Mao, *Talanta*, 2016, **161**, 205–210.
- 10 N. V. Guteneva, S. L. Znoyko, A. V. Orlov, M. P. Nikitin and P. I. Nikitin, *Microchim. Acta*, 2019, **186**, 621.
- 11 A. Moyano, M. Salvador, J. C. Martínez-García, V. Socoliuc, L. Vékás, D. Peddis, M. A. Alvarez, M. Fernández, M. Rivas and M. C. Blanco-López, *Anal. Bioanal. Chem.*, 2019, **411**, 6615–6624.
- 12 Y. Ha and I. Kim, *BioChip J.*, 2022, **16**, 351–365.
- 13 Y. Zhao, J. Sang, Y. Fu, J. Guo and J. Guo, *Analyst*, 2023, **148**, 3418–3431.
- 14 B. Cao, K. Wang, H. Xu, Q. Qin, J. Yang, W. Zheng, Q. Jin and D. Cui, *Sens. Actuators, A*, 2020, **312**, 112130.
- 15 K. Lee, S. Lee, J.-R. Kim and B. K. Cho, *J. Appl. Phys.*, 2009, **105**, 07E713.
- 16 C. Marquina, J. M. De Teresa, D. Serrate, J. Marzo, F. A. Cardoso, D. Saurel, S. Cardoso, P. P. Freitas and M. R. Ibarra, *J. Magn. Magn. Mater.*, 2012, **324**, 3495–3498.
- 17 A. W. Gani, W. Wei, R.-Z. Shi, E. Ng, M. Nguyen, M.-S. Chua, S. So and S. X. Wang, *Sci. Rep.*, 2019, **9**, 15615.
- 18 X.-H. Mu, H.-F. Liu, Z.-Y. Tong, B. Du, S. Liu, B. Liu, Z.-W. Liu, C. Gao, J. Wang and H. Dong, *Sens. Actuators, B*, 2019, **284**, 638–649.
- 19 H. Lei, K. Wang, X. Ji and D. Cui, *Sensors*, 2016, **16**, 2130.
- 20 B. Wang, T. Peng, Z. Jiang, J. Xu, J. Qu and X. Dai, *ACS Sens.*, 2023, **8**, 4512–4520.
- 21 The Magnetic Immuno-Chromatographic Test System by MagnaBioSciences, LLC, <https://www.magnabiosciences.com/technology.html>, accessed July 1, 2024.
- 22 J. Barnett, P. Wraith, J. Kiely, R. Persad, K. Hurley, P. Hawkins and R. Luxton, *Biosensors*, 2014, **4**, 204–220.
- 23 J. L. Marqués-Fernández, M. Salvador, J. C. Martínez-García, P. Fernández-Miaja, A. García-Arribas and M. Rivas, *Sensors*, 2023, **23**, 2372.
- 24 D. Lago-Cachon, M. Oliveira-Rodriguez, M. Rivas, M. C. Blanco-Lopez, J. C. Martinez-Garcia, A. Moyano, M. Salvador and J. A. Garcia, *IEEE Magn. Lett.*, 2017, **8**, 1–5.
- 25 M. H. F. Meyer, H.-J. Krause, M. Hartmann, P. Miethe, J. Oster and M. Keusgen, *J. Magn. Magn. Mater.*, 2007, **311**, 259–263.
- 26 A. García-Arribas, *Sensors*, 2020, **20**, 1961.
- 27 M. Salvador, Á. Gallo-Cordova, A. Moyano, J. C. Martínez-García, M. C. Blanco-López, M. Puerto Morales and M. Rivas, *Analyst*, 2020, **145**, 5905–5914.
- 28 B. D. Cullity and C. D. Graham, *Introduction to Magnetic Materials*, IEEE/Wiley, Hoboken, New Jersey, 2nd edn, 2009.
- 29 C. Pereira, A. M. Pereira, C. Fernandes, M. Rocha, R. Mendes, M. P. Fernández-García, A. Guedes, P. B. Tavares, J.-M. Grenèche, J. P. Araújo and C. Freire, *Chem. Mater.*, 2012, **24**, 1496–1504.
- 30 F. A. Tourinho, R. Franck and R. Massart, *J. Mater. Sci.*, 1990, **25**, 3249–3254.
- 31 L. Yang, L. Ma, J. Xin, A. Li, C. Sun, R. Wei, B. W. Ren, Z. Chen, H. Lin and J. Gao, *Chem. Mater.*, 2017, **29**, 3038–3047.
- 32 S. Díez-Villares, M. A. Ramos-Docampo, A. Da Silva-Candal, P. Hervella, A. J. Vázquez-Ríos, A. B. Dávila-Ibáñez, R. López-López, R. Iglesias-Rey, V. Salgueiriño and M. D. L. Fuente, *Adv. Healthcare Mater.*, 2021, **10**, 2101019.





- 33 L.-X. Yang, F. Wang, Y.-F. Meng, Q.-H. Tang and Z.-Q. Liu, *J. Nanomater.*, 2013, **2013**, 1–5.
- 34 G. Liu, B. Dai, Y. Ren and W. Zhang, *Results Phys.*, 2021, **26**, 104441.
- 35 G. Gnanaprakash, J. Philip and B. Raj, *Mater. Lett.*, 2007, **61**, 4545–4548.
- 36 C. N. Chinnasamy, B. Jeyadevan, O. Perales-Perez, K. Shinoda, K. Tohji and A. Kasuya, *IEEE Trans. Magn.*, 2002, **38**, 2640–2642.
- 37 O. Karaagac and H. Kockar, *J. Supercond. Novel Magn.*, 2011, **25**, 2777–2781.
- 38 R. Valenzuela, M. C. Fuentes, C. Parra, J. Baeza, N. Duran, S. K. Sharma, M. Knobel and J. Freer, *J. Alloys Compd.*, 2009, **488**, 227–231.
- 39 L. Li, K. Y. Mak, C. W. Leung, K. Y. Chan, W. K. Chan, W. Zhong and P. W. T. Pong, *Microelectron. Eng.*, 2013, **110**, 329–334.
- 40 A. Bee, R. Massart and S. Neveu, *J. Magn. Magn. Mater.*, 1995, **149**, 6–9.
- 41 R. B. Goldfarb and H. E. Bussey, *Rev. Sci. Instrum.*, 1987, **58**, 624.
- 42 D. Lago-Cachón, M. Rivas, J. C. Martínez-García, M. Oliveira-Rodríguez, M. C. Blanco-López and J. A. García, *J. Magn. Magn. Mater.*, 2017, **423**, 436–440.
- 43 P. Vermette, T. Gengenbach, U. Divisekera, P. A. Kambouris, H. J. Griesser and L. Meagher, *J. Colloid Interface Sci.*, 2003, **259**, 13–26.
- 44 A. Moyano, E. Serrano-Pertierra, M. Salvador, J. Martínez-García, Y. Piñeiro, S. Yañez-Vilar, M. González-Gómez, J. Rivas, M. Rivas and M. Blanco-López, *Biosensors*, 2020, **10**, 80.
- 45 C. Oliver and M. C. Jamur, *Immunocytochemical Methods and Protocols*, Humana Press, Totowa, NJ, 2010, vol. 588.
- 46 M. Salvador, J. L. Marqués-Fernández, J. C. Martínez-García, D. Fiorani, P. Arosio, M. Avolio, F. Brero, F. Balanean, A. Guerrini, C. Sangregorio, V. Socoliuc, L. Vekas, D. Peddis and M. Rivas, *Nanomaterials*, 2022, **12**, 205.
- 47 H. Ma, L. Guo, H. Zhang, Y. Wang, Y. Miao, X. Liu, M. Peng, X. Deng, Y. Peng and H. Fan, *ACS Appl. Bio Mater.*, 2022, **5**, 3067–3074.
- 48 V. Pilati, R. Cabreira Gomes, G. Gomide, P. Coppola, F. G. Silva, F. L. O. Paula, R. Perzynski, G. F. Goya, R. Aquino and J. Depeyrot, *J. Phys. Chem. C*, 2018, **122**, 3028–3038.
- 49 J. D. A. Gomes, M. H. Sousa, F. A. Tourinho, R. Aquino, G. J. Da Silva, J. Depeyrot, E. Dubois and R. Perzynski, *J. Phys. Chem. C*, 2008, **112**, 6220–6227.
- 50 S. Nigam, K. C. Barick and D. Bahadur, *J. Magn. Magn. Mater.*, 2011, **323**, 237–243.
- 51 M. E. De Sousa, M. B. Fernández Van Raap, P. C. Rivas, P. Mendoza Zélis, P. Girardin, G. A. Pasquevich, J. L. Alessandrini, D. Muraca and F. H. Sánchez, *J. Phys. Chem. C*, 2013, **117**, 5436–5445.
- 52 S. Laurent, D. Forge, M. Port, A. Roch, C. Robic, L. V. Elst and R. N. Muller, *Chem. Rev.*, 2008, **108**, 2064–2110.
- 53 R. Valenzuela, M. C. Fuentes, C. Parra, J. Baeza, N. Duran, S. K. Sharma, M. Knobel and J. Freer, *J. Alloys Compd.*, 2009, **488**, 227–231.
- 54 H. Zhang, D. Zeng and Z. Liu, *J. Magn. Magn. Mater.*, 2010, **322**, 2375–2380.
- 55 S. V. Andreev, M. I. Bartashevich, V. I. Pushkarsky, V. N. Maltsev, L. A. Pamyatnykh, E. N. Tarasov, N. V. Kudrevatykh and T. Goto, *J. Alloys Compd.*, 1997, **260**, 196–200.
- 56 E. C. Stoner and E. P. Wohlfarth, *Philos. Trans. R. Soc. London*, 1948, **240**, 599–642.
- 57 R. Aquino, J. Depeyrot, M. H. Sousa, F. A. Tourinho, E. Dubois and R. Perzynski, *Phys. Rev. B*, 2005, **72**, 184435.
- 58 R. Chantrell, J. Popplewell and S. Charles, *IEEE Trans. Magn.*, 1978, **14**, 975–977.
- 59 F. H. Sánchez, P. Mendoza Zélis, M. L. Arciniegas, G. A. Pasquevich and M. B. Fernández Van Raap, *Phys. Rev. B*, 2017, **95**, 134421.
- 60 A. Omelyanchik, S. Villa, M. Vasilakaki, G. Singh, A. M. Ferretti, A. Ponti, F. Canepa, G. Margaritis, K. N. Trohidou and D. Peddis, *Nanoscale Adv.*, 2021, **3**, 6912–6924.
- 61 I. J. Bruvera, P. Mendoza Zélis, M. Pilar Calatayud, G. F. Goya and F. H. Sánchez, *J. Appl. Phys.*, 2015, **118**, 184304.
- 62 J. S. Micha, B. Dieny, J. R. Régnard, J. F. Jacquot and J. Sort, *J. Magn. Magn. Mater.*, 2004, **272–276**, E967–E968.
- 63 Y. A. Urian, J. J. Atoche-Medrano, L. T. Quispe, L. León Félix and J. A. H. Coaquira, *J. Magn. Magn. Mater.*, 2021, **525**, 167686.
- 64 M. Modestino, A. Galluzzi, M. Sarno and M. Polichetti, *Materials*, 2023, **16**, 4246.
- 65 M. S. Andersson, *J. Nanosci. Nanotechnol.*, 2019, **19**, 4903–4910.
- 66 M. Knobel, W. C. Nunes, L. M. Socolovsky, E. De Biasi, J. M. Vargas and J. C. Denardin, *J. Nanosci. Nanotechnol.*, 2008, **8**, 2836–2857.
- 67 C. R. Alves, R. Aquino, J. Depeyrot, F. A. Tourinho, E. Dubois and R. Perzynski, *J. Mater. Sci.*, 2007, **42**, 2297–2303.
- 68 P. García-Acevedo, M. A. González-Gómez, Á. Arnosa-Prieto, L. De Castro-Alves, Y. Piñeiro and J. Rivas, *Adv. Sci.*, 2023, **10**, 2203397.
- 69 M. Pack, H. Hu, D.-O. Kim, X. Yang and Y. Sun, *Langmuir*, 2015, **31**, 7953–7961.
- 70 D. Mampallil and H. B. Eral, *Adv. Colloid Interface Sci.*, 2018, **252**, 38–54.
- 71 S. Kunikin, A. Zakinyan and Y. Dikansky, *J. Magn. Magn. Mater.*, 2019, **483**, 178–182.
- 72 C. Rosano, P. Arosio and M. Bolognesi, *Biomol. Eng.*, 1999, **16**, 5–12.
- 73 A. Jain, A. Barve, Z. Zhao, W. Jin and K. Cheng, *Mol. Pharm.*, 2017, **14**, 1517–1527.
- 74 Avidin and NeutrAvidin™ Biotin-Binding Proteins and Conjugates, <https://www.thermofisher.com/document-connect/document-connect.html?url=https://assets.thermofisher.com/TFS-Assets%2FMSG%2Fmanuals%2Fmp00887.pdf>.
- 75 M. H. Jazayeri, H. Amani, A. A. Pourfatollah, H. Pazoki-Toroudi and B. Sedighimoghaddam, *Sens. Bio-Sens. Res.*, 2016, **9**, 17–22.
- 76 K. E. Sapsford, K. M. Tyner, B. J. Dair, J. R. Deschamps and I. L. Medintz, *Anal. Chem.*, 2011, **83**, 4453–4488.

